Revisiting the Foundations of Subsurface Scattering

Gladimir V. G. Baranoski Aravind Krishnaswamy Bradley Kimmel

Natural Phenomena Simulation Group, School of Computer Science, University of Waterloo, Canada
Technical Report CS-2003-45

Abstract

Despite the significant advances in rendering, we are far from being able to automatically generate realistic and predictable images of organic materials such as plant and human tissues. Creating convincing pictures of these materials is usually accomplished by carefully adjusting rendering parameters. A key issue in this context is the simulation of subsurface scattering. Current algorithmic models usually rely on scattering approximations based on the use of phase functions, notably the Henyey-Greenstein phase function and its variations, which were not derived from biophysical principles of any organic material, and whose parameters have no biological meaning. In this report, we challenge the validity of this approach for organic materials. Initially, we present an original chronology of the use of these phase functions in tissue optics simulations, which highlights the pitfalls of this approach. We then demonstrate that a significant step toward predictive subsurface scattering simulations can be given by replacing it by a more efficient and accurate data oriented approach. Our investigation is supported by comparisons involving the original measured data that motivated the application of phase functions in tissue subsurface scattering simulations. We hope that the results of our investigation will help strengthen the biophysical basis required for the predictive rendering of organic materials.

CR Categories: I.3.7 [Computing Methodologies]: Computer Graphics—3D Graphics

Keywords: biophysically-based rendering, subsurface scattering, phase function, light transport, radiative transfer, algorithmic simulations, Monte Carlo methods.

1 Introduction

Since the beginning of computer graphics in the late 1960's, researchers have been mostly concerned with the process of creating realistic images of the world around us. One of the most important stages of this process is the simulation of light interaction with matter. Efforts in this area resulted in predictable images of inorganic materials. More recently, organic materials, such as plant and human tissues [Hanrahan and Krueger 1993; Jensen et al. 2001; Ng and Li 2001; Stam 2001], whose scattering behavior is characterized by a highly significant subsurface component, have been carefully rendered to generate believable images. For these materials, however, one may ask a couple of questions. First, are the models of light interaction with organic materials accurate from a biophysical point of view? Second, are these simulations predictive?

In order to answer these questions, one needs to perform comparisons between modeled and measured data. In general such comparisons are not performed, and the employed validation approach is based solely on the visual inspection of the generated images. For applications in several areas (*e.g.*, entertainment and games industries) believable images are usually good enough. However, if the models were described by biophysically meaningful parameters and the algorithms and resulting images were accurate representations of light transport processes, the simulations could be used in a predictive manner [Greenberg et al. 1997]. This would make the process of realistic image synthesis more intuitive [Arvo 1995a]. Furthermore, this biophysically-based approach has a broader range of applications, including not only believable picture making, but also scientific and medical applications such as the noninvasive diagnosis of skin phototraumas and tumors [Tuchin 2000; Cotton 1997].

Accuracy and computational time are often conflicting issues in biophysically-based rendering. Although the main goal in this area is the design of accurate and efficient models, sometimes it is difficult to obtain this perfect combination. In order to achieve a higher level of accuracy, it may be necessary to add complexity to a model, which in turn may negatively affect its computational performance. However, this is not always the case. In fact, we are going to show in this report that one may be able to obtain more accurate and efficient representations of biophysical phenomena in many cases by removing undue complexity.

The core of any rendering algorithm is formed by the scattering functions. These are also called phase functions when applied to volumetric scattering [Glassner 1995]. The purpose of this report is to revisit the foundations of subsurface scattering simulations, including the widespread application of the Henyey-Greenstein phase function (henceforth referred to as HGPF) [Henyey and Greenstein 1941] in the modeling of light transport in tissue. We are going to show through comparisons with actual measured data that it negatively affects both accuracy and efficiency of subsurface scattering simulations. We hope that the results of our investigation will help to demonstrate that a significant step toward predictive tissue optics models can be given by using experimental data directly, instead of functions which came to play just as an attempt to fit such data.

The remainder of this report is organized as follows. The next section provides an overview of the HGPF formulation and terminology. Section 3 presents an original chronology of tissue optics research which resulted in the questionable application of the HGPF in tissue subsurface scattering simulation. Section 4 describes the experimental investigation set-up used to demonstrate the pitfalls of the HGPF approximations and the advantages of a data oriented approach. Section 5 presents the results of these comparisons and discusses their practical implications. Finally, Section 6 concludes the report emphasizing the the need of a multi-disciplinary effort to advance this important area of research.

2 HGPF: Fundamentals

In this section we review the fundamental aspects of the HGPF. A detailed discussion of phase functions is beyond the scope of this report. Adequate reviews are available in the books by van de Hulst [van de Hulst 1980a; van de Hulst 1980b; van de Hulst 1981] and Ishimaru [Ishimaru 1997a; Ishimaru 1997b].

2.1 Phase Functions

When light hits a particle with an index of refraction different from its environment (Figure 1), the light is scattered. The direction of scattering is characterized by the angle θ at which the light is bent and an azimuth angle β. Let E_0 be the energy flux per unit area of the incident light, E the energy flux per unit area of the scattered light in a point at a distance r from the particle, and k the wave number defined by $k = 2\pi\lambda$, where λ is the wavelength in the surrounding medium. Since E must be proportional to E_0 and r^{-2} [van de Hulst 1981], we may write:

$$E = \frac{E_0 \Phi(\theta, \beta)}{k^2 r^2}, \tag{1}$$

where $\Phi(\theta, \beta)$ is a dimensionless function ($\frac{F}{k^2}$ is an area) of the direction but not of r. The relative values of E may be plotted in a polar diagram, also called *scattering diagram*, as a function of θ in a fixed plane through the direction of incidence.

Let the total energy scattered in all directions be equal to the energy of the incident light falling on an area A_{sca} (also called scattering cross section [van de Hulst 1981], which is defined as:

$$A_{sca} = \frac{1}{k^2} \int_S \Phi(\theta, \beta) d\omega, \tag{2}$$

where $d\omega = \sin\theta d\theta d\beta$ is the differential solid angle and the integral is taken over the entire sphere, S.

When $\Phi(\theta, \beta)$ is divided by $k^2 A_{sca}$, another function of direction, the *phase function*, here denoted by ϕ, is obtained. The phase function has no physical dimension. It represents the amount of scattered flux (power), *i.e.*, the *scattering profile* of a given particle. For example, a phase function represented by $\phi(\vec{v}, \vec{v_s})$ describes the amount of light scattered from the direction denoted by the unit vector $\vec{v}$ into the direction $\vec{v_s}$. In astrophysics this function is treated as a probability distribution, and its normalization requires the integral over all angles to equal the unity:

$$\int_S \phi(\vec{v}, \vec{v_s}) d\omega = 1. \tag{3}$$

This condition does not permit the phase function to describe absorption of light by the particle, only the scattering distribution. Thus $\phi(\vec{v}, \vec{v_s}) d\omega$ is the probability that a photon incident from the direction given by the vector $\vec{v}$ will leave in the differential unit of solid angle in the direction given by the vector $\vec{v_s}$ [Prahl 1988], *i.e.*, it represents a single scattering event. The probability of light scattering through an angle θ after n scattering events is given by a multiple-scattered phase function, a concept initially used by Tessendorf and Wasdon to simulate multiple scattering in clouds, and recently applied by Premoze *et al.* [Premoze et al. 2003] in the rendering of objects with subsurface scattering.

The name "phase function" has no relation to the phase of the electromagnetic wave (light). It has its origins in astronomy, where it refers to lunar phases [Ishimaru 1997a]. Coincidentally, one of the most widely used phase functions in radiative transfer theory, and the focus of our investigation, the HGPF, was designed aiming at astrophysical applications, namely the study of diffuse radiation in galaxies [Henyey and Greenstein 1941].

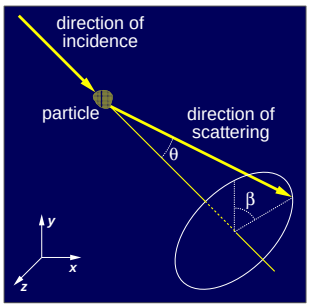

Figure 1: *Sketch describing the scattering angles.*

2.2 HGPF: Formulation and Terminology

The HGPF was presented by Henyey and Greenstein to approximate Mie scattering in their study of diffuse radiation in galaxies [Henyey and Greenstein 1941]. It is important to note, however, that a theoretical derivation for this phase function was not provided by Henyey and Greenstein [1941].

The HGPF is given by:

$$\phi(g, \theta) = \frac{1 - g^2}{(1 + g^2 - 2g\cos\theta)^{\frac{3}{2}}}, \tag{4}$$

where the parameter g is defined as the integral over all angles of the phase function multiplied by the cosine of the angle θ. The HGPF is actually a function of *three* parameters: g, θ and β. It just happens that an azimuthal symmetry of the phase function is assumed, *i.e.*, the function is constant with respect to β. By varying the parameter g, called asymmetry factor, in the range $-1 \leq g \leq 1$, it is possible to characterize HGPFs ranging from a completely backward-throwing to a completely forward-throwing form (Figure 2).

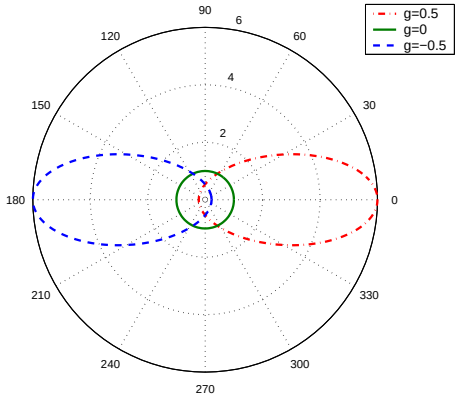

Figure 2: *Scattering diagrams illustrating different scattering profiles provided by the HGPF.*

The HGPF as defined in Equation 4 cannot, however, be used to describe simultaneous forward and backward lobes which are typical in many cases of Mie scattering as well as Rayleigh scattering [Witt 1977]. For this reason, astrophysicists proposed variations based on the superposition of two HGPFs [Uesugi et al. 1971; Kattawar 1975; Witt 1977]:

$$\phi(g_1, g_2, \theta, u) = u\phi(g_1, \theta) + (1 - u)\phi(g_2, \theta), \tag{5}$$

where $\phi(g_1, \theta)$ and $\phi(g_2, \theta)$ each are of the form given by Equation 4, and u is a suitably chosen uniformly distributed random number on the interval $[0, 1]$. Figure 3 illustrate three scattering profiles provided by the two-term HGPF.

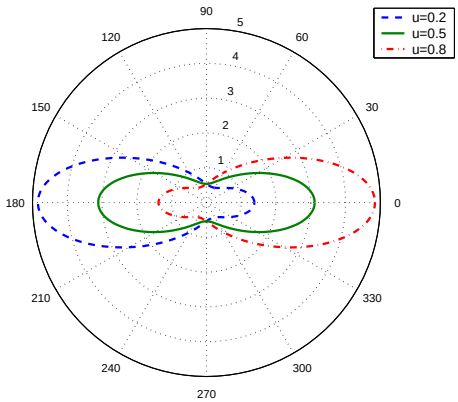

Figure 3: *Scattering diagrams illustrating different scattering profiles provided by the two-term HGPF with* $g_1 = 0.5$ *and* $g_2 = -0.5$.

The asymmetry factor is oftentimes called anisotropy factor. We employ the former term throughout this report since we consider the use of the term "anisotropy" inappropriate. Recall that the function has no dependency on the azimuthal angle. Furthermore, there is no direct relationship between this parameter and a macroscopic anisotropic behavior of a given material, *i.e.*, a dependence on both the polar and the azimuthal angles measured from the material's normal and used to define the direction of incidence of the incoming light.

3 HGPF in Tissue Subsurface Scattering: Chronology and Problems

The HGPF is neither based on a mechanistic theory of scattering [Jacques et al. 1987] nor does its asymmetry factor have any biological meaning. Two important questions then come to mind. Why is the HGPF extensively used in rendering of both inorganic and organic materials? What problems may result from its usage? In order to answer these questions we need to go back in time, and track down the sequence of events that culminated in its use in tissue subsurface scattering simulations.

In 1976, bioengineers [Petersen et al. 1976] attempted to use the HGPF to approximate Mie scattering in blood. Their investigation did not show a good agreement between the HGPF approximation and the experimental data, however.

Later on, Bruls and van der Leun [1984] performed goniometric measurements of the scattering profile of two types of skin tissues, namely stratum corneum and epidermis (Table 1). The resulting data correspond to the amount of radiation transmitted into a solid angle $\Delta\omega$, centered around the direction given by θ, as a fraction of the total radiation transmitted at perpendicular irradiation. The measured scattering distributions were in the range given by $0^\circ \leq \theta \leq 62.5^\circ$, and the cumulative fractions of the transmitted energy were expressed as:

$$C_i(\theta) = \frac{\int_{0^\circ}^{\theta_i + 2.5^\circ} E(\theta) \sin\theta d\theta}{\int_{0^\circ}^{62.5^\circ} E(\theta) \sin\theta d\theta} \times 100\%, \tag{6}$$

where E corresponds to the energy flux per unit area of the scattered radiation, and $\theta_i = 5i$ for $i = 0, ..., 12$.

angle	Stratum Corneum					Epidermis			
θ	254	302	365	436	546	302	365	436	546
$2.5°$	9.3	11.6	14.8	17.6	20.6	1.3	1.7	2.6	4.0
$7.5°$	40.2	45.1	50.1	55.2	60.2	9.4	11.9	16.1	22.5
$12.5°$	59.2	63.0	66.8	70.9	75.2	20.8	24.8	30.8	39.7
$17.5°$	71.1	73.7	76.5	79.1	82.3	33.2	37.5	43.6	52.5
$22.5°$	79.2	80.6	82.3	84.1	86.5	45.5	49.0	54.5	62.4
$27.5°$	85.1	85.6	86.3	87.6	89.4	56.9	59.8	63.9	70.2
$32.5°$	89.3	89.3	89.4	90.3	91.5	66.9	69.2	71.9	76.7
$37.5°$	92.5	92.2	92.0	92.5	93.4	75.7	77.4	79.0	82.4
$42.5°$	95.0	94.5	94.1	94.4	95.0	83.2	84.2	85.0	87.2
$47.5°$	96.9	96.5	96.0	96.1	96.5	89.3	89.8	90.1	91.4
$52.5°$	98.4	98.0	97.6	97.6	97.8	94.1	94.3	94.3	94.9
$57.5°$	99.4	99.2	98.9	99.0	99.0	97.7	97.8	97.8	97.9
$62.5°$	100.0	100.0	100.0	100.0	100.0	100.0	100.0	100.0	100.0

Table 1: *Scattering profiles of stratum corneum and epidermis tissues measured at 436nm and 546nm, and presented in terms of the cumulative fractions (%), $C(\theta)$, of radiation transmitted within a certain angle θ with respect to the tissue's normal (redrawn from Bruls and van der Leun [1984]).*

In their paper, Bruls and van der Leun [1984] suggested the scattering profile of organic tissues could be approximated by single particle phase functions:

> *We compared epidermal profiles with results from multiple scattering theory. Van de Huslt (1980) provides elaborate computations of scattering profiles of layers filled with particles, on the basis of a single particle scattering phase function that ranges from diffuse to very forward oriented. Our epidermal profiles are compatible with profiles from his Table 35.*

The table from van de Hulst [1980a] mentioned above, corresponds to the HGPF. In 1987, Jacques et al. [1987] followed Bruls and van der Leun's suggestion, and tried to approximate the measured scattering profile of another skin tissue, namely dermis, using HGPF with $g = 0.81$. Yoon et al. [1987] used similar g values for human aorta. The experiments on dermis and aorta tissues were aimed at specific medical applications and conducted with a HeNe laser (632.8nm). Motivated by these works, Prahl [1988] proposed a Monte Carlo based algorithm to model light transport in tissue during laser irradiation. Although this Monte Carlo based approach was used before to study light propagation in tissue [Wilson and Adam 1983], Prahl's algorithmic formulation, to the best of our knowledge, was the first proposed to use the HGPF to compute the scattering of photons in organic tissues. In order to compute the trajectories of the scattered photons, Prahl [1988] used a warping function provided by Witt [1977], which was obtained by setting:

$$\xi_1 = 2\pi \int_{-1}^{\cos\theta} \phi(cos\theta', g) d\theta', \tag{7}$$

and finding upon integration that

$$\cos\theta = \frac{1}{2g}\left\{1 + g^2 - \left[\frac{1-g^2}{1-g+2g\xi_1}\right]^2\right\}, \tag{8}$$

where ξ_1 is an uniformly distributed random number on the interval $[0, 1]$. An alternative detailed derivation of this warping function is available in Appendix A. For symmetric scattering (g=0) the expression $\cos\theta = 2\xi_1 - 1$ should be used [Prahl et al. 1989]. Since an azimuthal symmetry of the phase function is assumed, the azimuthal angle can be generated using $\beta = 2\pi\xi_2$, where ξ_2 is a random number uniformly distributed on the interval $[0, 1]$.

In 1989, biomedical researchers [van Gemert et al. 1989] attempted to fit the HGPF to the goniometric measurements of Bruls and van der Leun [1984], and used a least squares method to determine suitable values for g. After that, it was assumed that the HGPF could be used to approximate the scattering profile of organic tissues regardless of wavelength. This assumption has not been questioned up to the present time. In fact, the use of HGPF in analytical and algorithmic subsurface scattering simulation became widespread in many areas involving tissue optics [Tuchin 2000], and new comprehensive goniometric measurements for tissue subsurface scattering were not performed.

In 1993, graphics researchers [Hanrahan and Krueger 1993] introduced the algorithmic formulation for the simulation of tissue subsurface scattering proposed by Prahl [1988] to the graphics literature. This included the use of the HGPF described above. In their examples, Hanrahan and Krueger used $g = 0.81$ for dermis and $g = 0.79$ for epidermis. They did not include stratum corneum in their skin representation. Since then, the HGPF has also been used in computer graphics applications involving subsurface scattering simulations [Jensen et al. 1999; Jensen et al. 2001; Pharr and Hanrahan 2000; Premoze et al. 2003; Ng and Li 2001; Stam 2001].

Are there indeed any problems with this use of HGPF in tissue subsurface scattering simulations? First, recall the asymmetry factor g has no direct connection with the underlying biophysical phenomena. Second, as described above, the HGPF was initially meant to be used in tissue optics just as a function to fit multiple scattering data of skin measured at specific wavelengths. As we are going to show in the following sections, the HGPF approximations deviate from the measured data.

The accuracy level of the HGPF approximations decreases even more when they are used to describe the subsurface behavior of materials characterized by a dominant reflective-refractive scattering (caused by internal structures much larger than the wavelength of light) such as plant tissues [Govaerts et al. 1996]. In these applications the selection of values for g is made on a trial and error basis, and it has neither an empirical nor a theoretical foundation.

In short, we believe that the HGPF approximations cannot be simply generalized and applied to any tissue and any wavelength. Furthermore, we maintain that the use of this function adds undue complexity to algorithmic subsurface scattering simulations. In the following sections we will demonstrate that these simulations can be performed with a higher accuracy/time ratio using measured data directly.

4 Experimental Investigation Set-up

In order to determine the accuracy of scattering profiles obtained using the HGPF, we compared these profiles with the experimental goniometric data (Table 1) provided by Bruls and van der Leun [1984]. For the HGPF asymmetry factors we considered the values determined by van Gemert et al. [1989], which have been commonly used in algorithmic subsurface scattering simulations. One might argue that the fitting approach used by van Gemert et al. [1989] to determine the g values could be replaced by another one, which could result into better approximations for the profiles. For this reason, we also used g values obtained by applying the RMS error metric [Glassner 1995] to the measured data. We have experimented with other error metric approaches, namely absolute and relative error metrics (Appendix B). We selected the results obtained using the RMS error metric for presentation since the RMS g values provide a closer visual match to the results obtained using the measured data.

The asymmetry factors used in our comparisons are presented in Table 1. They correspond to the measured data for the visible range of the light spectrum (436nm and 546nm) provided by Bruls and van der Leun [1984]. The complete set of asymmetry factors obtained using the RMS, absolute and relative error metrics, for measured data for both the ultraviolet and visible ranges [Bruls and van der Leun 1984], are presented in Tables 4 and 5 (Appendix B).

To determine the asymmetry factors, we initially subtracted the consecutive cumulative fractions of the transmitted radiation (Equation 6) to get $F_\tau^{(i)} = C_i - C_{i-1}$, for $i = 1, \ldots, 12$, and $F_\tau^{(0)} = C_0$. Thus,

$$F_\tau^{(i)} = \frac{\int_{\max(0^\circ, \theta_i - 2.5^\circ)}^{\theta_i + 2.5^\circ} E(\theta)\, d\omega}{\int_{0^\circ}^{62.5^\circ} E(\theta)\, d\omega}, \tag{9}$$

where $\theta_i = 5i$, for $i = 0, \ldots, 12$.

Next, to obtain the HGPF data to be compared to the data from Equation 9, we computed the following cumulative density function:

$$P(\theta < \theta') = \int_0^{\theta'} \phi_g(\omega)\, d\omega, \tag{10}$$

and we obtained

$$C_{g,i} = \frac{P(\theta < \theta_i + 2.5^\circ)}{P(\theta < 62.5^\circ)}, \tag{11}$$

where $\theta_i = 5i$, for $i = 0, \ldots, 12$. We then performed the operation $F_\tau^{(g,i)} = C_{g,i} - C_{g,i-1}$ for $i \geq 1$ and $F_\tau^{(g,0)} = C_{g,0}$.

The RMS error metric $\epsilon_{RMS}(g)$ used to compare the $F_\tau^{(i)}$ and the $F_\tau^{(g,i)}$, for $i = 0, \ldots, 12$, is given by:

$$\epsilon_{RMS}(g) = \sqrt{\frac{1}{m} \sum_{i=0}^{m-1} \left(F_\tau^i - F_\tau^{(g,i)} \right)^2}, \tag{12}$$

where $m = 13$. We applied the Nelder-Mead simplex search algorithm [Lagarias et al. 1998] to minimize $\epsilon_{RMS}(g)$ over $g \in [-1, 1]$ to obtain the most suitable asymmetry factor.

asymmetry factors	Stratum Corneum		Epidermis	
source	436	546	436	546
RMS error metric	0.935	0.943	0.761	0.821
van Gemert et al. [1989]	0.900	0.917	0.748	0.781

Table 2: *Asymmetry factors obtained by fitting the HGPF to scattering profiles of stratum corneum and epidermis tissues measured at 436nm and 546nm.*

We believe that a data oriented approach provides approximations with a higher accuracy/time ratio. In order to confirm this assertion we implemented a randomized table look-up algorithm. The scattering angles are stored in a table, whose access indices correspond to the measured fractions of scattered radiation. For each photon we generate a uniformly distributed random number on the interval $[0, 1]$. We then multiply this number by the table size. The integer part of the resulting value is used to access the corresponding scattering angle stored in the table. The table size is limited by the granularity of the measured goniometric data, which consists of values with one decimal digit accuracy. Thus, for each wavelength considered, we used a table with 1000 entries. The intermediate data values were obtained through interpolation, another design choice based on the granularity of the measured goniometric data. For the sake of simplicity and due to the lack of information about the scattering behavior between data points we used linear interpolation.

We performed two sets of experiments. In both sets we generate N samples (photons) represented by random numbers uniformly distributed on the interval $[0, 1]$.

In the first set (with $N = 10^5$), for each photon, we determined the scattering angle given by Equation 8 with the g values presented in Table 2, and the scattering angle given by the randomized table look-up technique. The number of samples per measured scattering angle for

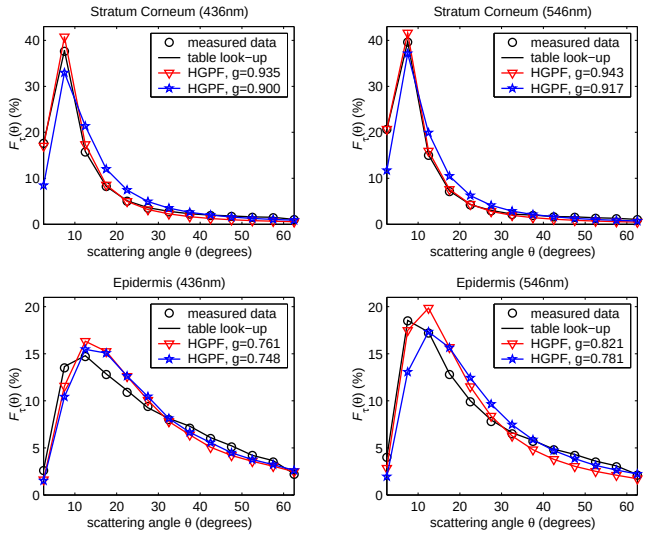

Figure 4: *Comparison between reconstructed transmitted radiation curves and goniometric measured data for the stratum corneum and epidermis tissues.*

Approximation Approach	Stratum Corneum				Epidermis			
	436		546		436		546	
	max	avg	max	avg	max	avg	max	avg
HGPF, with g provided by van Gemert et al. [1989]	51.96	27.08	47.71	27.76	42.40	14.04	51.24	16.09
HGPF, with g provided by RMS error metric	53.03	23.08	52.79	21.90	35.24	14.57	30.02	18.43
randomized table look-up	7.22	3.32	8.48	4.17	3.45	1.56	3.25	1.70

Table 3: *Relative error figures, namely maximum and average values (%), for the approximation methods (with $N = 10^5$) with respect to the goniometric data for the stratum corneum and epidermis measured at 436nm and 546nm.*

each approach was recorded and the comparisons performed. Since the experimental data was limited to $62.5°$, the scattering angles given by the HGPF beyond this value were discarded and not taken into account into the sample summations.

The second set of experiments (with $N = 10^6$) followed a similar protocol. It was performed through the implementation of a virtual goniometer, which was used to compute the BTDF (bidirectional transmittance distribution function) associated with the scattering profiles obtained using the HGPF and the randomized table look-up technique. Since an azimuthal symmetry of the phase function is assumed (Section 2.2), the BTDF values were computed on the plane given by the incident light and the tissue's normal. The BTDF values corresponding to the measured data, denoted by f_τ^i, for $i = 0, \ldots, 12$, were calculated using:

$$f_t(\vec{\omega_i}, \vec{\omega_t}) = \frac{F_\tau^{(i)}}{\vec{\omega_t} \ \cos\theta}, \tag{13}$$

where $\vec{\omega_i}$ and $\vec{\omega_t}$ correspond to the indicence and transmissive solid angles. Similarly, to compute the BTDF corresponding to HGPF data we replaced $F_\tau^{(i)}$ by $F_\tau^{(g,i)}$ in the equation above.

Organic tissues, such as the stratum corneum and epidermis, are usually considered as part of a whole material, *i.e.*, human skin. Moreover, there are other factors affecting subsurface scattering such as the absorption of light by pigments [Krishnaswamy and Baranoski 2004]. However, one may use simple abstractions, called "phantom materials", to expand the scope of visual observations. Such abstractions are extensively used in biomedical research [Cotton 1997; Shimada et al. 2001a; Shimada et al. 2001b], and similar abstractions have also being used in computer graphics [Arvo 1995a; Arvo 1995b]. In our investigation these phantom materials are represented by thin translucent sheets with a forward scattering behavior simulated using the HGPF (with the values given in Table 2) and the randomized table look-up technique. The resulting images were obtained using a standard path tracing algorithm without post-processing signal smoothing [Glassner 1995].

5 Results and Discussion

The results of the first set of experiments considering the stratum corneum data are shown in Figure 4 (top row). As expected, the randomized table look-up technique provides the closest match to the measured data, which can also be observed in Table 3. It is worth noting that the use of asymmetry factors given by the RMS error metric provides a closer approximation than the values provided by van Gemert et al. [1989], which have been used in computer graphics simulations.

The results of the first set of experiments considering the epidermis data are given in Figure 4 (bottom row). In this case, the disparity between the HGPF approximations and the measured data, which increases for data measured at 546nm, can be observed. Again, a more

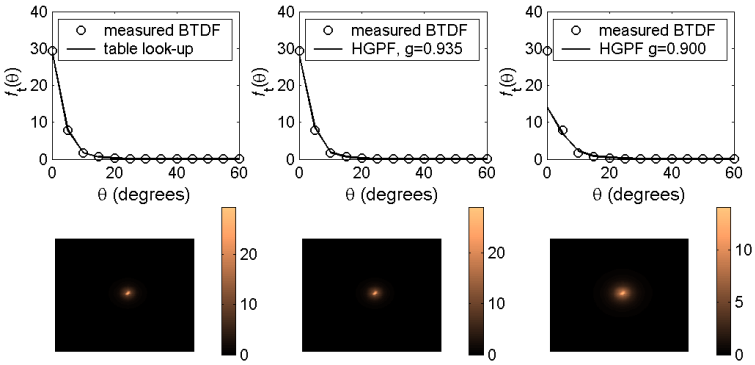

Figure 5: *Reconstructed BTDF values for the stratum corneum tissue at 436nm. Left: table look-up. Middle: HGPF (with RMS g). Right: HGPF (with g provided by van Gemert et al. [1989]). Top row: Cartesian plot. Bottom row: orthographic projection of the scattering diagram.*

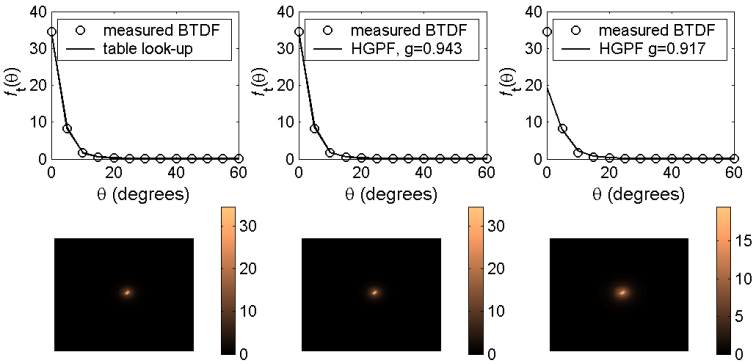

Figure 6: *Reconstructed BTDF values for the stratum corneum tissue at 546nm. Left: table look-up. Middle: HGPF (with RMS g). Right: HGPF (with g provided by van Gemert et al. [1989]). Top row: Cartesian plot. Bottom row: orthographic projection of the scattering diagram.*

accurate approximation is provided by the randomized table look-up technique. It introduces even smaller errors with respect to the epidermis data set, which can also be observed in Table 3.

Figures 5 and 6 present the results of the second set of experiments with stratum corneum data. They show that the quantitative discrepancies between BTDF values obtained using the randomized table look-up and the reconstructed BTDF values obtained using the HGPF are small, with closer approximations being obtained using asymmetry factors provided by the RMS error metric.

The results of the second set of experiments with epidermis data, which are presented in Figures 7 and 8, show noticeable quantitative and qualitative discrepancies between the BTDF values obtained using the randomized table look-up and the BTDF values obtained using the HGPF. For these experiments, closer approximations were also obtained using asymmetry factors provided by the RMS error metric.

In short, our experiments indicate that the randomized table look-up provides a more accurate agreement with the measured data. The magnitude of the discrepancies between this approach and the HGPF approach may, however, have a different significance depending on the application. For rendering frameworks aimed at scientific and medical applications, it is clearly relevant. For example, the epidermis contains an important skin pigment, melanin. The amount of light absorbed by this pigment affects not only the skin appearance [Tsumura et al. 2003], but also the visual diagnosis of medical conditions such as melanomas at early stages [Cotton 1997]. This amount depends on the path-length of the incoming photons, which is in turn affected by the tissue's scattering properties.

For rendering frameworks aimed at believable picture making applications, the visual effects caused by the different approaches may become more pronounced or negligible depending on the illumination conditions (*e.g.*, collimated or diffuse incident beams), the structural characteristics of the materials (*e.g.*, thickness) and perception issues associated with the human visual system [Greenberg et al. 1997]. Figures 9 and 11 illustrate this aspect through images of phantom materials generated using the stratum corneum and the epidermis data respectively. For example, although the experiments presented earlier indicated small discrepancies between the approximation approaches with respect to the stratum corneum data, the images shown in Figure 9 present remarkable differences in terms of the phantom material's translucency. Such differences can vary depending, for instance on the distance between the materials' interfaces as illustrated in Figure 10. On the other hand, despite the evident quantitative and qualitative discrepancies between the approximation approaches with respect to the epidermis data verified in the experiments presented earlier, the images present in Figure 11 (top row) do not noticeable differences in terms of the phantom material's translucency.

Regarding the computational costs of each approach, recall that the HGPF formulation includes an expensive fractional exponentiation. For example, for the SGI MIPS R14000 processors used in our experiments, this operation is performed five times slower than a randomized table look-up operation. On the other hand, the data oriented approach requires additional storage space. For instance, the tables used in

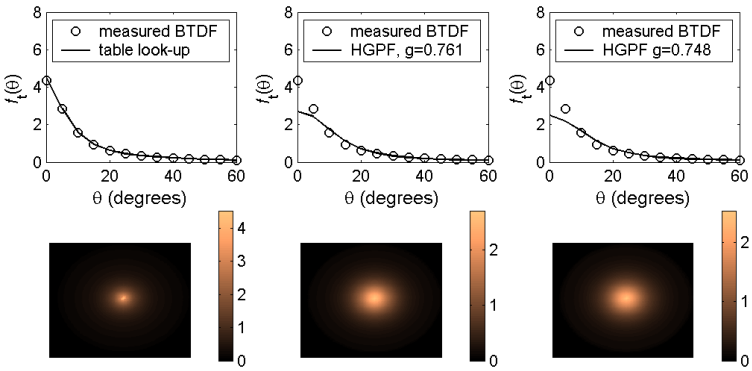

Figure 7: *Reconstructed BTDF values for the epidermis tissue at 436nm. Left: table look-up. Middle: HGPF (with RMS g). Right: HGPF (with g provided by van Gemert et al. [1989]). Top row: Cartesian plot. Bottom row: orthographic projection of the scattering diagram.*

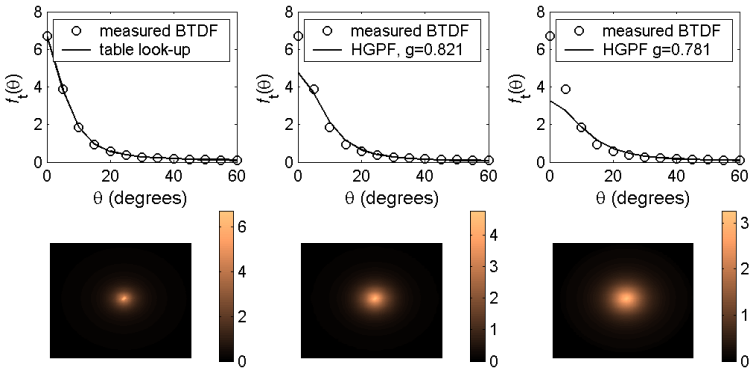

Figure 8: *Reconstructed BTDF values for the epidermis tissue at 546nm. Left: table look-up. Middle: HGPF (with RMS g). Right: HGPF (with g provided by van Gemert et al. [1989]). Top row: Cartesian plot. Bottom row: orthographic projection of the scattering diagram.*

our experiments occupy 36Kb of memory. Taking into account the size of the memories available nowadays and their decreasing price, ony may consider this figure quite acceptable. Hence, we believe that the data oriented approach provides a more advantageous trade-off between computational costs and accuracy, while avoiding the introduction of undue complexity in algorithmic subsurface scattering simulations.

A legitimate criticism of our investigation is that our comparisons are limited to few wavelengths. This limitation is imposed by the lack of measured spectral subsurface data. We should note, however, that this aspect highlights the pitfalls of the generalized use of HGPF in algorithmic subsurface scattering simulations. Considering wavelengths for which there is no measure data available, the selection of asymmetry factors, which have no biophysical meaning, is purely ad hoc.

One could argue that the asymmetry factors for these wavelengths can be computed by interpolating HGPF values obtained from available data. Recall that the randomized table look-up technique, besides the introduction of smaller errors, has the important advantage of avoiding the expensive fractional exponentiation in the HGPF formulation. Hence, we can obtain values with a higher accuracy/time ratio by interpolating values given by the randomized table look-up technique.

Usually picture making applications, such those found in entertainment and games industries, do not require high fidelity. The major disadvantage of using the HGPF in these applications is the introduction of undue complexity in the rendering frameworks and the lack of predictability. However, scientific applications, such as noninvasive optical-tissue diagnostics [Mourant et al. 1998], demand a high level of accuracy. In order to increase the accuracy in these applications, one could select another phase function to fit the scattering data, *e.g.*, the Reynolds-McCormick [1980; 1988] or the Dunn and Richards-Kortum [1996] phase functions. These functions, however, have the same drawbacks as the HGPF, namely ad hoc parameters, expensive formulations and an accuracy arguably smaller than a data oriented approach.

Besides the direct effect on the predictability of algorithmic simulations, the selection of asymmetry factors may have further theoretical implications in subsurface scattering. For example, Jensen and Buhler [2002] used a diffusion approximation to improve the efficiency of their subsurface scattering simulations. They state that this approximation has been shown by Furutso [1980] to be accurate when $\frac{\sigma_a}{\sigma_a+\sigma_s} << 1-g^2$, where σ_a and σ_s correspond to the material's absorption and scattering coefficients respectively. Clearly, in order to apply this relationship, one needs to know the values of its terms, which in turn come from measured data, especially the asymmetry factor g. As shown by our experiments, the value of g may result from a fitting approach that does not match the measured data accurately, *i.e.*, it may be itself an approximation.

Incidentally, there are two additional accuracy issues related to the application of the diffusion approximation [Jensen and Buhler 2002] to describe the subsurface scattering of organic materials, in particular human skin tissues. First, the diffusion approximation is not suitable when the scattering is mostly in the forward direction [Furutso 1980; Flock et al. 1989; Yoon et al. 1989]. As we have shown in this report, the measurements performed by Bruls and van der Leun [1984] demonstrate that both the stratum corneum and the epidermis tissues are highly forward scattering media. Second, the diffusion theory is not applicable when the absorption coefficient is not significantly smaller than the

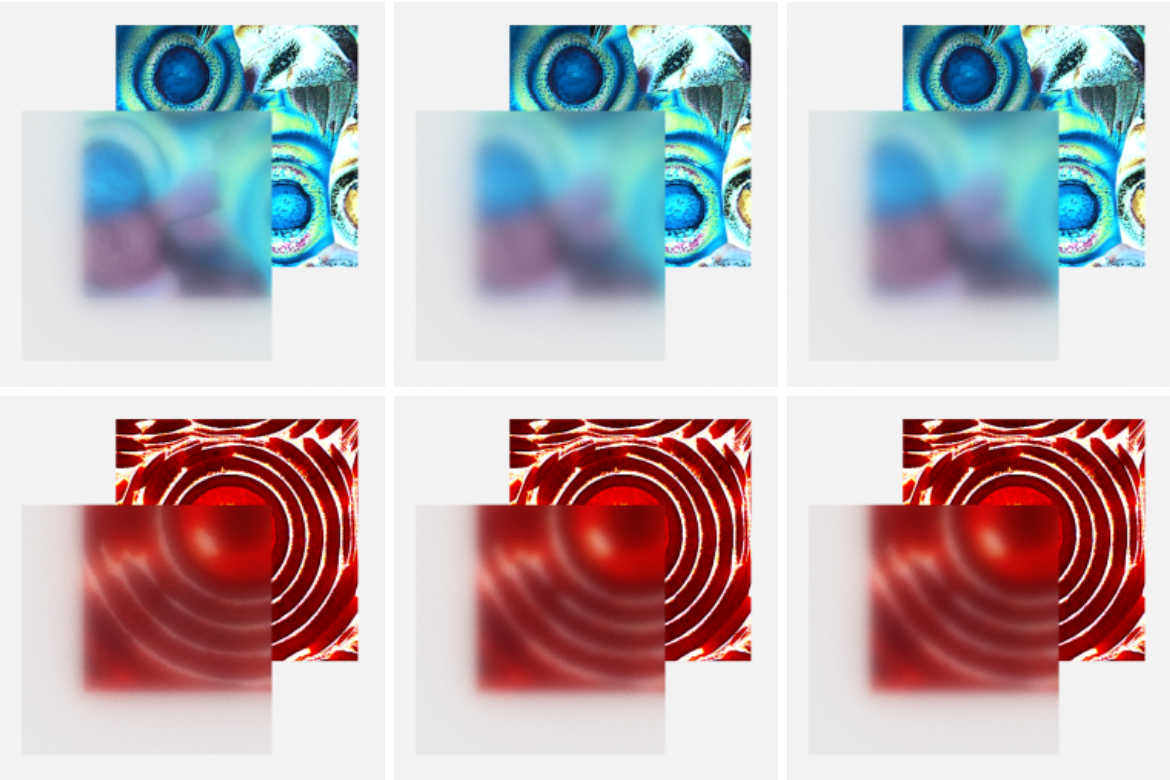

Figure 9: *Images of a phantom material with a scattering behavior simulated using data corresponding to the scattering behavior of the stratum corneum tissue measured at 436nm (top row) and 546nm (bottom row). Left column: applying the randomized table look-up. Middle column: applying the HGPF with the asymmetry factors provided by the RMS error metric. Right column: applying the HGPF with the asymmetry factors provided by van Gemert et al. [1989]. Surfaces are separated by 0.9 length units.*

scattering coefficient for turbid media [Sardar and Levy 1998; Steinke and Shepherd 1988; Yoon et al. 1989]. Human skin is characterized by relatively high light absorption [Krishnaswamy and Baranoski 2004; Parsad et al. 2003; Thody et al. 1991], due to pigments such as melanin particles which have a significant absorption cross section [Chedekel 1995]. It is worth noting that the diffusion approximation is well suited for media such as thick fogs and clouds [Furutso 1980], since they present a scattering behavior that it is dominated by forward scattering and their absorption of light in the visible range (due to the presence of water) is negligible. It is also worth noting that the diffusion approximation for large absorption has been investigated by Meador and Weaver [1979]. However, their approach is restricted to diffuse incidence [Yoon et al. 1989].

6 Conclusion and Future Work

Phase functions, such as the HGPF and its variations, were originally used in tissue subsurface scattering simulations to fit data measured at specific wavelengths. Since then, their application has been extended to different organic materials despite the lack of supporting measured data and the fact that their parameters have no biological meaning. The investigation described in this report demonstrates that a data oriented approach not only increases the accuracy and efficiency of algorithmic subsurface scattering simulations, but also contributes to their predictability since the simulations are no longer controlled by arcane parameters.

Our investigation also highlights a key issue in biophysically-based rendering: data availability. Many graphics researchers have been working to minimize this problem, and a substantial amount of goniometric surface data has been collected and analyzed. Besides being scarcer, goniometric subsurface data may also contain some degree of random noise, which is usually not filtered out by the approximation methods. Therefore, in order to develop predictive subsurface scattering algorithms, we believe that efforts should also be focused on the reliable measurement of multispectral subsurface data.

As multispectral databases become available, memory space may become an issue, specially for a field researcher or a forensic scientist with a hand-held computing device of limited storage. In these situations, numerical techniques, such as Principal Component Analysis (PCA) [Jolliffe 2002], can be used to reduce the dimensionality of such databases as it has been done in colorimetry for many years [Vrhel et al. 1994; Imai et al. 1996]. These techniques not only provide compact databases, but also support fast addition of new spectral data.

As future work we intend to explore the biophysical characteristics of organic materials to increase the efficiency of PCA techniques within subsurface scattering simulation frameworks. We also intend to extend our investigation to ultra-violet spectra, and take advantage of graphics hardware to increase the efficiency of the subsurface scattering algorithms.

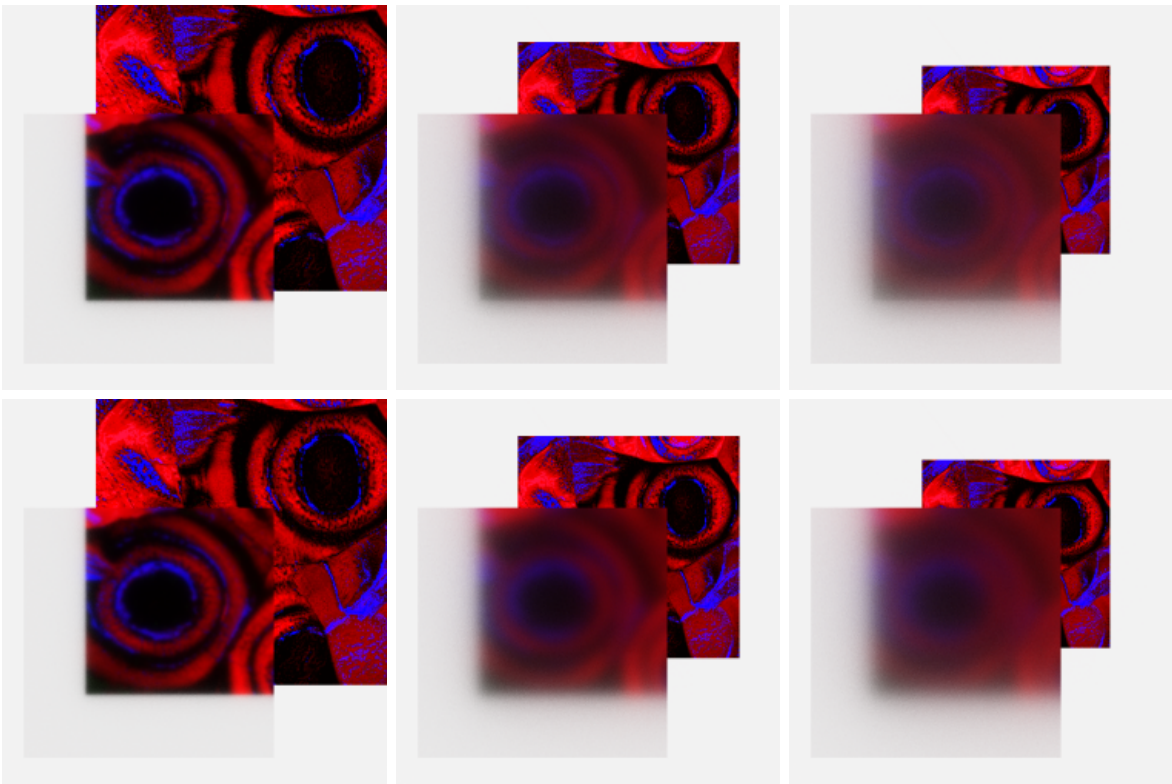

Figure 10: *Images of a phantom material with a scattering behavior simulated using data corresponding to the scattering behavior of the stratum corneum tissue measured at 546nm. Top row: applying the randomized table look-up. Bottom row: applying the HGPF with the asymmetry factor provided by the RMS error metric. The surfaces are separated by 0.2 (left column), 1.2 (middle column) and 1.8 (right column) length units.*

References

ARVO, J. 1995. *Analytic Methods for Simulated Light Transport*. PhD thesis, Yale University.

ARVO, J. 1995. Applications of irradiance tensors to the simulation of non-lambertian phenomena. In *SIGGRAPH, Annual Conference Series*, 335–342.

BRULS, W., AND VAN DER LEUN, J. 1984. Forward scattering properties of human epidermal layers. *Photochem. Photobiol. 40*, 231–242.

CHEDEKEL, M. 1995. Photophysics and photochemistry of melanin. In *Melanin: Its Role in Human Photoprotection*, Valdenmar Publishing Company, Overland Park, Kansas, USA, M. C. L. Zeise and T. Fitzpatrick, Eds., 11–22. 2223b.

COTTON, S. 1997. A noninvasive skin imaging system. Tech. Rep. CSR-97-03, School of Computer Science, The University of Birmingham.

DUNN, A., AND RICHARDS-KORTUM, R. 1996. Three-dimensional computation of light scattering from cells. *IEEE Selected Topics in Quantum Electronics 2*, 898–905.

FLOCK, S. T., PATTERSON, M. S., WILSON, B. C., AND WYMAN, D. R. 1989. Monte Carlo modeling of light propagation in highly scattering tissues - I: Model predictions and comparison with diffusion theory. *IEEE Transactions on Biomedical Engineering 36*, 12 (December), 1162–1168.

FURUTSO, K. 1980. Diffusion equation derived from space-time transport equation. *Journal of the Optical Society of America 70*, 360.

GLASSNER, A. 1995. *Principles of Digital Image Synthesis*. Morgan Kaufmann Publishers, Inc, San Francisco.

GOVAERTS, Y., JACQUEMOUD, S., VERSTRAETE, M., AND USTIN, S. 1996. Three-dimensional radiation transfer modeling in a dycotyledon leaf. *Applied Optics 35*, 33 (November), 6585–6598.

GREENBERG, D., ARVO, J., LAFORTUNE, E., TORRANCE, K., FERWERDA, J., WALTER, B., TRUMBORE, B., SHIRLEY, P., PATTANAIK, S., AND FOO, S. 1997. A framework for realistic image synthesis. In *SIGGRAPH, Annual Conference Series*, 477–494.

HANRAHAN, P., AND KRUEGER, W. 1993. Reflection from layered surfaces due to subsurface scattering. In *SIGGRAPH, Annual Conference Series*, 165–174.

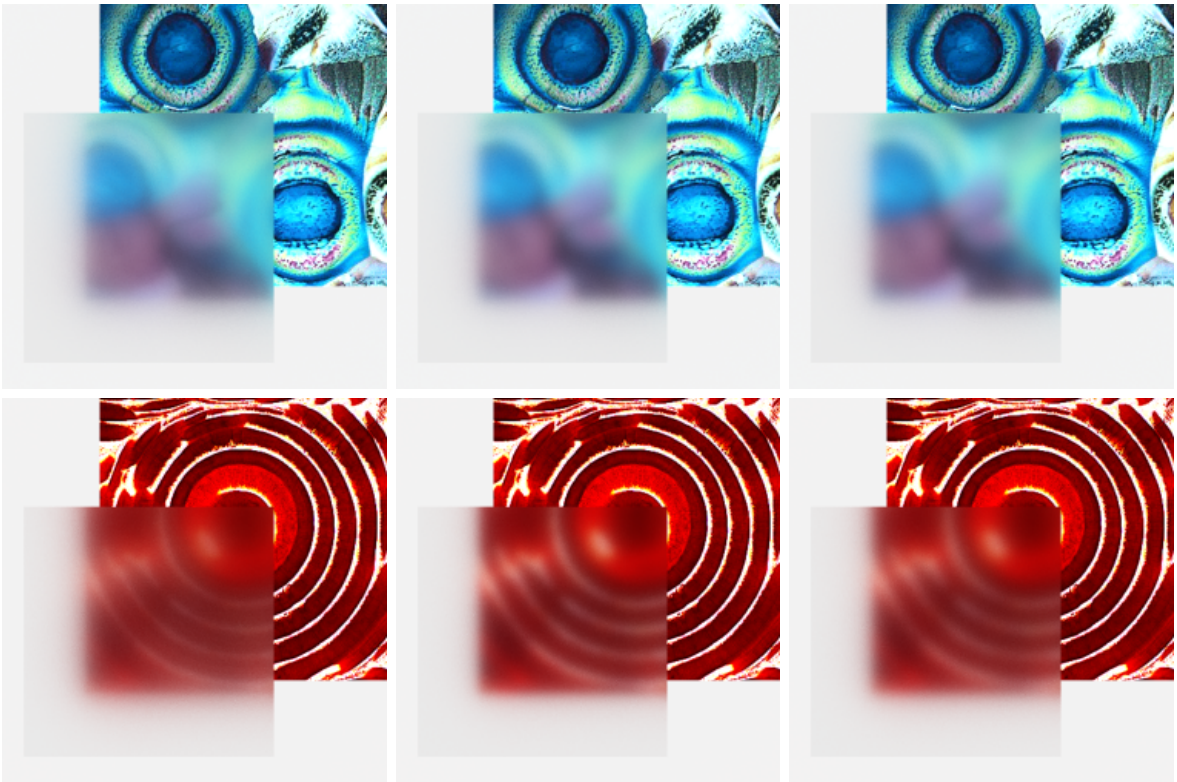

Figure 11: *Images of a phantom material with a scattering behavior simulated using data corresponding to the scattering behavior of the epidermis tissue measured at 436nm (top row) and 546nm (bottom row). Left column: applying the randomized table look-up. Middle column: applying the HGPF with the asymmetry factors provided by the RMS error metric. Right column: applying the HGPF with the asymmetry factors given by van Gemert et al. [1989]. Surfaces are separated by 0.3 length units.*

HENYEY, L., AND GREENSTEIN, J. 1941. Diffuse radiation in the galaxy. *Astrophysics Journal 93*, 70–83.

IMAI, F., TSUMURA, N., HANEISHI, H., AND MIYAKE, Y. 1996. Principal component analysis of skin color and its application to colorimetric reproduction on CRT display and hardcopy. *Journal of Image Science and Technology 40*, 422–430.

ISHIMARU, A. 1997. *Wave Propagation and Scattering in Random Media*, 2nd ed., vol. 1. IEEE Press, New York.

ISHIMARU, A. 1997. *Wave Propagation and Scattering in Random Media*, 2nd ed., vol. 2. IEEE Press, New York.

JACQUES, S., ALTER, C., AND PRAHL, S. 1987. Angular dependence of HeNe laser light scattering by human dermis. *Lasers in Life Sciences 1*, 4, 309–333.

JENSEN, H., AND BUHLER, J. 2002. A rapid hierarchical rendering technique for translucent materials. In *SIGGRAPH, Annual Conference Series*, 576–581.

JENSEN, H., LEGAKIS, J., AND DORSEY, J. 1999. Rendering of wet materials. In *Rendering Techniques'1999 (Proceedings of the 10th Eurographics Rendering Workshop)*, Springer-Verlag, Granada, D. Lischinski and G. W. Larson, Eds., 281–289.

JENSEN, H., MARSCHNER, S., LEVOY, M., AND HANRAHAN, P. 2001. A practical model for subsurface light transport. In *SIGGRAPH, Annual Conference Series*, 511–518.

JOLLIFFE, I. 2002. *Principal Component Analysis*, 2nd ed. Springer-Verlag, New York.

KATTAWAR, G. 1975. A three-parameter analytic phase function for multiple scattering calculations. *Journal of Quantitative Spectroscopy and Radiative Transfer 15*, 839–849.

KRISHNASWAMY, A., AND BARANOSKI, G. 2004. A study on skin optics. Tech. Rep. CS-2004-01, School of Computer Science, University of Waterloo, Canada, January.

LAGARIAS, J., REEDS, J., WRIGHT, M., AND WRIGHT, P. 1998. Convergence properties of the Nelder-Mead simplex method in low dimensions. *SIAM Journal of Optimization 9*, 1, 112–147.

MEADOR, W., AND WEAVER, W. 1979. Diffusion approximation for large absorption in radiative transfer. *Applied Optics 18*, 1204–1208.

MOURANT, J., FREYER, J., HIELSCHER, A., EICK, A., SHEN, D., AND JOHNSON, T. 1998. Mechanisms of light scattering from biological cells relevant to noninvasive optical-tissue diagnostics. *Applied Optics 37*, 16 (June), 3586–3593.

NG, C., AND LI, L. 2001. A multi-layered reflection model of natural human skin. In *Computer Graphics International 2001*, 249–256.

PARSAD, D., WAKAMATSU, K., KANWAR, A., KUMAR, B., AND ITO, S. 2003. Eumelanin and phaeomelanin contents of depigmented and repigmented skin in vitiligo patients. *British Journal of Dermatology 149*, 624–626.

PETERSEN, G., MCCORMICK, N., AND REYNOLDS, L. 1976. Transport calculations for light scattering in blood. *Biophysical Journal 16*, 199–207.

PHARR, M., AND HANRAHAN, P. 2000. Monte Carlo evaluation of non-linear scattering equations for subsurface reflection. In *SIGGRAPH, Annual Conference Series*, 75–84.

PRAHL, S., KEIJZER, M., JACQUES, S., AND WELCH, A. 1989. A Monte Carlo model of light propagation in tissue. *SPIE Institute Series IS 5*, 102–111.

PRAHL, S. 1988. *Light Transport in Tissue*. PhD thesis, The University of Texas at Austin.

PREMOZE, S., ASHIKHMIN, M., AND SHIRLEY, P. 2003. Path integration for light transport in volumes. In *Eurographics Symposium on Rendering*, P. Christensen and D. Cohen-Or, Eds., 75–84.

REYNOLDS, L., AND MCCORMICK, N. 1980. Approximate two-parameter phase function for light scattering. *Journal of the Optical Society of America 70*, 1206.

SARDAR, D., AND LEVY, L. 1998. Optical properties of whole blood. *Lasers in Medical Science 13*, 106–111.

SHIMADA, M., YAMADA, Y., ITOH, M., AND YATAGAI, T. 2001. Melanin and blood concentration in human skin studied by multiple regression analysis: assessment by Monte Carlo simulation. *Physics in Medicine and Biology 46*, 2397–2406.

SHIMADA, M., YAMADA, Y., ITOH, M., AND YATAGAI, T. 2001. Melanin and blood concentration in human skin studied by multiple regression analysis: experiments. *Physics in Medicine and Biology 46*, 2385–2395.

STAM, J. 2001. An illumination model for a skin layer bounded by rough surfaces. In *Rendering Techniques'2001 (Proceedings of the 12th Eurographics Rendering Workshop)*, Springer-Verlag, London, P. M. Hanrahan and W. Purgathofer, Eds., 39–52.

STEINKE, J., AND SHEPHERD, A. 1988. Diffusion model of the optical absorbance of whole blood. *Journal of the Optical Society of America 5*, 6, 813–822.

THODY, A., HIGGINS, E., WAKAMATSU, K., ITO, S., BURCHILL, S., AND MARKS, J. 1991. Pheomelanin as well as eumelanin is present in human dermis. *Journal of Investigative Dermatology 97*, 340–344.

TSUMURA, N., OJIMA, N., SATO, K., SHIRAISHI, M., SHIMIZU, H., NABESHIMA, H., AKAZAKI, S., HORI, K., AND MIYAKE, Y. 2003. Image-based skin color and texture analysis/synthesis by extracting hemoglobin and melanin information in the skin. *ACM Transactions on Graphics 22*, 3, 770–779.

TUCHIN, V. 2000. *Tissue Optics Light Scattering Methods and Instruments for Medical Diagnosis*. The International Society for Optical Engineering, Bellingham, Washington.

UESUGI, A., IRVINE, W., AND KAWATA, Y. 1971. Formation of absorption spectra by diffuse reflection from a semi-infinite planetary atmosphere. *Journal of Quantitative Spectroscopy and Radiative Transfer 11*, 797–808.

VAN DE HULST, H. 1980. *Multiple Light Scattering: Tables, Formulas, and Applications*, vol. 1. Academic Press, New York.

VAN DE HULST, H. 1980. *Multiple Light Scattering: Tables, Formulas, and Applications*, vol. 2. Academic Press, New York.

VAN DE HULST, H. 1981. *Light Scattering by Small Particles*, 2nd ed. Dover Publications Inc., New York.

VAN GEMERT, M., JACQUES, S., STERENBORG, H., AND STAR, W. 1989. Skin optics. *IEEE Transactions on Biomedical Engineering 36*, 12, 1146–1154.

VRHEL, M., GERSHON, R., AND IWAN, L. 1994. Measurement and analysis of object reflectance spectra. *Color Research and Application 19*, 1, 4–9.

WILSON, B., AND ADAM, G. 1983. A Monte Carlo model for the absorption and flux distributions of light in tissue. *Medical Physics 10*, 824–830.

WITT, A. 1977. Multiple scattering in reflection nebulae. I. a Monte Carlo approach. *The Astrophysical Journal Supplement Series 15* (September), 1–6.

YOON, G., WELCH, A., MOTAMEDI, M., AND VAN GEMERT, M. 1987. Development and application of three-dimensional light distribution model for laser irradiated tissue. *IEEE Journal of Quantum Electronics QE-23*, 1721–1733.

YOON, G., PRAHAL, S., AND WELCH, A. 1989. Accuracies of the diffusion approximation and its similarity relations for laser irradiated biological media. *Applied Optics 28*, 12, 2250–2255.

Appendix A: HGPF Warping Function

The HGPF, ϕ, is a function of *two* angles: θ and β. That is, $\phi/\int_S \phi$ is the probability density function over the entire sphere, S. Note that $\phi/\int_0^\pi \phi(\theta)d\theta$ is *not* the probability density function for θ over $[0,\pi]$. Since an azimuthal symmetry of the phase function is assumed, *i.e.*, the function is constant with respect to β, the azimuthal angle can be generated using $2\pi\xi_2$, where ξ_2 is a random number uniformly distributed on the interval $[0,1]$. To generate θ, we need to invert the cumulative density function for θ: $P(\theta<\theta')$. This can be expressed as

$$P(\theta<\theta') = \frac{1}{K}\int_{\theta<\theta'} \phi(\theta,\beta)d\omega, \tag{14}$$

where $K=\int_S \phi(\theta,\beta)d\omega$ is the constant that enforces unit area for probability density.

Expanding (14) yields:

$$\begin{aligned} P(\theta<\theta') &= \frac{1}{K}\int_0^{2\pi}\int_0^{\theta'} \frac{1-g^2}{(1+g^2-2g\cos\theta)^{3/2}}\sin\theta\, d\theta\, d\beta \\ &= \frac{1-g^2}{K}\int_0^{2\pi} d\beta \int_0^{\theta'} \frac{\sin\theta\, d\theta}{(1+g^2-2g\cos\theta)^{3/2}} \\ &= \frac{2\pi}{K}(1-g^2)\int_0^{\theta'} \frac{\sin\theta\, d\theta}{(1+g^2-2g\cos\theta)^{3/2}}. \end{aligned}$$

Let $u=1+g^2-2g\cos\theta$. Then $du=2g\sin\theta\, d\theta$ and u ranges from $1+g^2-2g=(1-g)^2$ to $1+g^2-2g\cos\theta'$ as θ ranges from 0 to θ'.

Now, we have:

$$\begin{aligned} P(\theta<\theta') &= \frac{\pi}{Kg}(1-g^2)\int_{(1-g)^2}^{1+g^2-2g\cos\theta'} u^{-\frac{3}{2}}\, du \\ &= \frac{-2\pi}{Kg}(1-g^2)u^{-\frac{1}{2}}\Big|_{(1-g)^2}^{1+g^2-2g\cos\theta'}, \end{aligned}$$

which results in:

$$P(\theta<\theta') = \frac{2\pi}{Kg}(1-g^2)\left(\frac{1}{1-g} - \frac{1}{\sqrt{1+g^2-2g\cos\theta'}}\right). \tag{15}$$

Noting that $P(\theta<\pi)=1$, we can derive K as follows:

$$\begin{aligned} K &= \frac{2\pi}{g}(1-g^2)\left(\frac{1}{1-g} - \frac{1}{\sqrt{1+g^2-2g\cos\pi}}\right) \\ &= \frac{2\pi}{g}(1-g^2)\left(\frac{1}{1-g} - \frac{1}{\sqrt{1+g^2+2g}}\right) \\ &= \frac{2\pi}{g}(1-g^2)\left(\frac{1}{1-g} - \frac{1}{\sqrt{(1+g)^2}}\right) \\ &= \frac{2\pi}{g}(1-g^2)\left(\frac{1}{1-g} - \frac{1}{1+g}\right) \\ &= \frac{2\pi}{g}(1-g^2)\frac{1+g-(1-g)}{1-g^2} \\ &= \frac{2\pi}{g}\cdot 2g \\ &= 4\pi. \end{aligned}$$

Substituting back into (15) yields

$$P(\theta<\theta') = \frac{1-g^2}{2g}\left(\frac{1}{1-g} - \frac{1}{\sqrt{1+g^2-2g\cos\theta'}}\right). \tag{16}$$

To generate θ', we let $P(\theta < \theta') = \xi_1$, where ξ_1 is an uniformly distributed random number on the interval $[0, 1]$, and solve for θ'. Thus:

$$\begin{aligned}
& \xi_1 = \frac{1-g^2}{2g}\left(\frac{1}{1-g} - \frac{1}{\sqrt{1+g^2-2g\cos\theta'}}\right) \\
\Rightarrow \quad & \frac{1}{\sqrt{1+g^2-2g\cos\theta'}} = \frac{1}{1-g} - \frac{2g\xi_1}{1-g^2} \\
\Rightarrow \quad & \frac{1}{\sqrt{1+g^2-2g\cos\theta'}} = \frac{1+g-2g\xi_1}{1-g^2} \\
\Rightarrow \quad & \sqrt{1+g^2-2g\cos\theta'} = \frac{1-g^2}{1+g-2g\xi_1} \\
\Rightarrow \quad & 1+g^2-2g\cos\theta' = \left(\frac{1-g^2}{1+g-2g\xi_1}\right)^2 \\
\Rightarrow \quad & \cos\theta' = \frac{1}{2g}\left(1+g^2-\left(\frac{1-g^2}{1+g-2g\xi_1}\right)^2\right).
\end{aligned}$$

In summary, to generate a random direction distributed according to the HGPF and represented by the pair (θ, ϕ), we use the warping function:

$$(\theta, \beta) = \left(\cos^{-1}\left(\frac{1}{2g}\left\{1+g^2-\left[\frac{1-g^2}{1+g-2g\xi_1}\right]^2\right\}\right), 2\pi\xi_2\right). \tag{17}$$

Appendix B: Error Metrics Used to Compute the Asymmetry Factors

Besides the RMS error metric (Equation 12), we have experimented with two other error metric approaches, namely the absolute error metric:

$$\epsilon_{ABS}(g) = \frac{1}{m}\sum_{i=0}^{m-1}\left|F_\tau^i - F_\tau^{(g,i)}\right|, \tag{18}$$

and the relative error metric

$$\epsilon_{REL}(g) = \frac{1}{m}\sum_{i=0}^{m-1}\left|\frac{F_\tau^i - F_\tau^{(g,i)}}{F_\tau^i}\right| \times 100\%. \tag{19}$$

The complete set of asymmetry factors obtained using the RMS, absolute and relative error metrics, for measured data for both the ultraviolet and visible ranges [Bruls and van der Leun 1984], are presented in Tables 4 and 5.

Error Metrics	254	302	365	436	546
RMS error	0.89558	0.90965	0.92293	0.93445	0.94257
Absolute error	0.89154	0.90206	0.92417	0.93589	0.94237
Relative error	0.88925	0.89858	0.91074	0.92172	0.94059

Table 4: *Asymmetry factors obtained by fitting the HGPF to scattering profiles of the stratum corneun tissue measured at 254nm, 302nm, 365nm, 436nm and 546nm by Bruls and van der Leun [1984].*

Error Metrics	302	365	436	546
RMS error	0.68071	0.71297	0.76079	0.82053
Absolute error	0.67503	0.70637	0.73890	0.82780
Relative error	0.68932	0.70637	0.73890	0.78818

Table 5: *Asymmetry factors obtained by fitting the HGPF to scattering profiles of the epidermis tissue measured at 302nm, 365nm, 436nm and 546nm by Bruls and van der Leun [1984].*

Figures 12 to 20 show comparisons between reconstructed cumulative transmitted radiation curves (obtained using asymmetry factors computed applying the error metrics described above) and goniometric measured data [Bruls and van der Leun 1984].

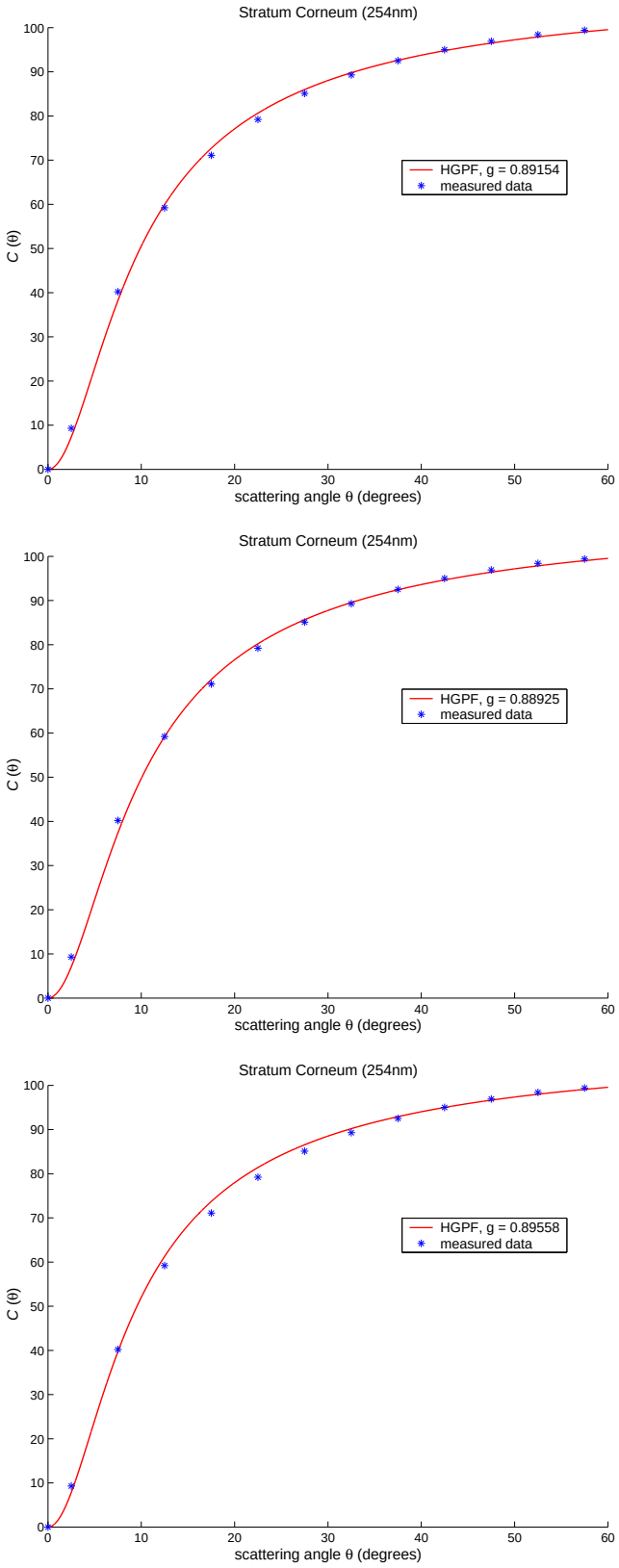

Figure 12: *Asymmetry factor computed using: absolute error (top), relative error (middle) and RMS error metric (bottom).*

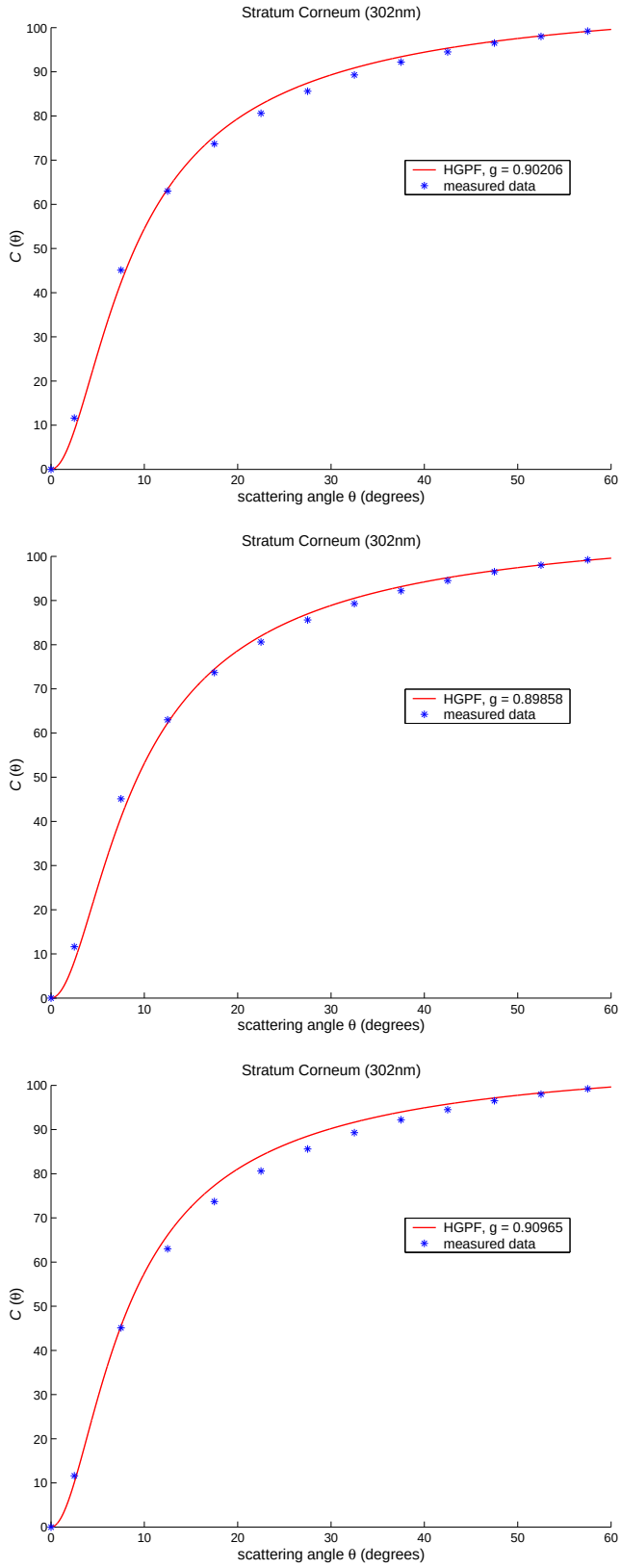

Figure 13: *Asymmetry factor computed using: absolute error (top), relative error (middle) and RMS error metric (bottom).*

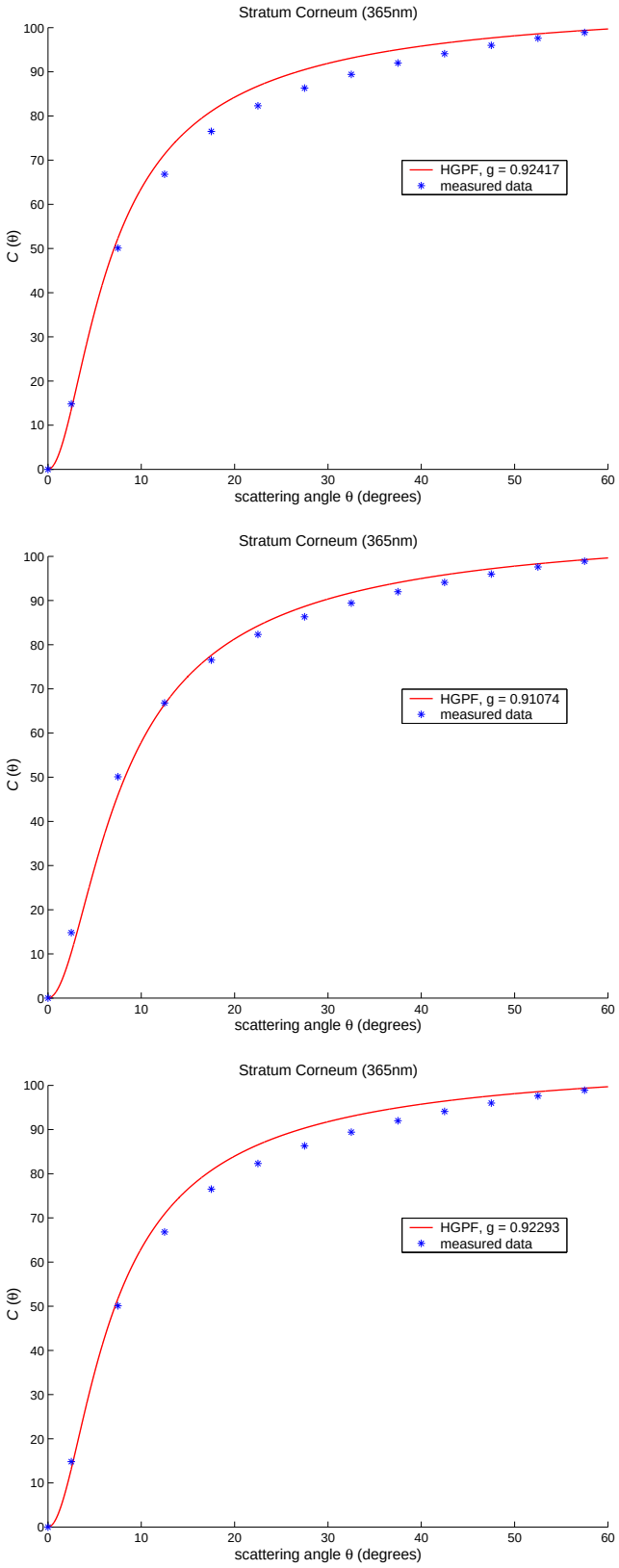

Figure 14: *Asymmetry factor computed using: absolute error (top), relative error (middle) and RMS error metric (bottom).*

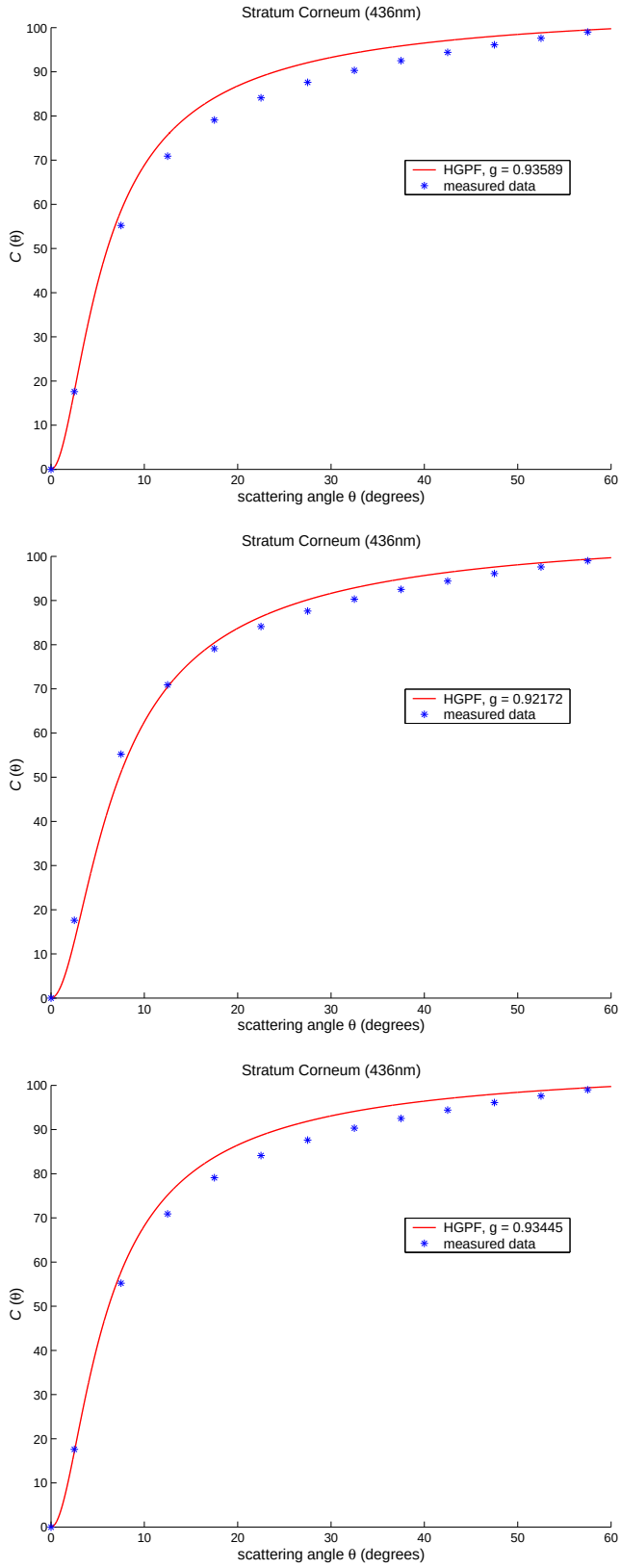

Figure 15: *Asymmetry factor computed using: absolute error (top), relative error (middle) and RMS error metric (bottom).*

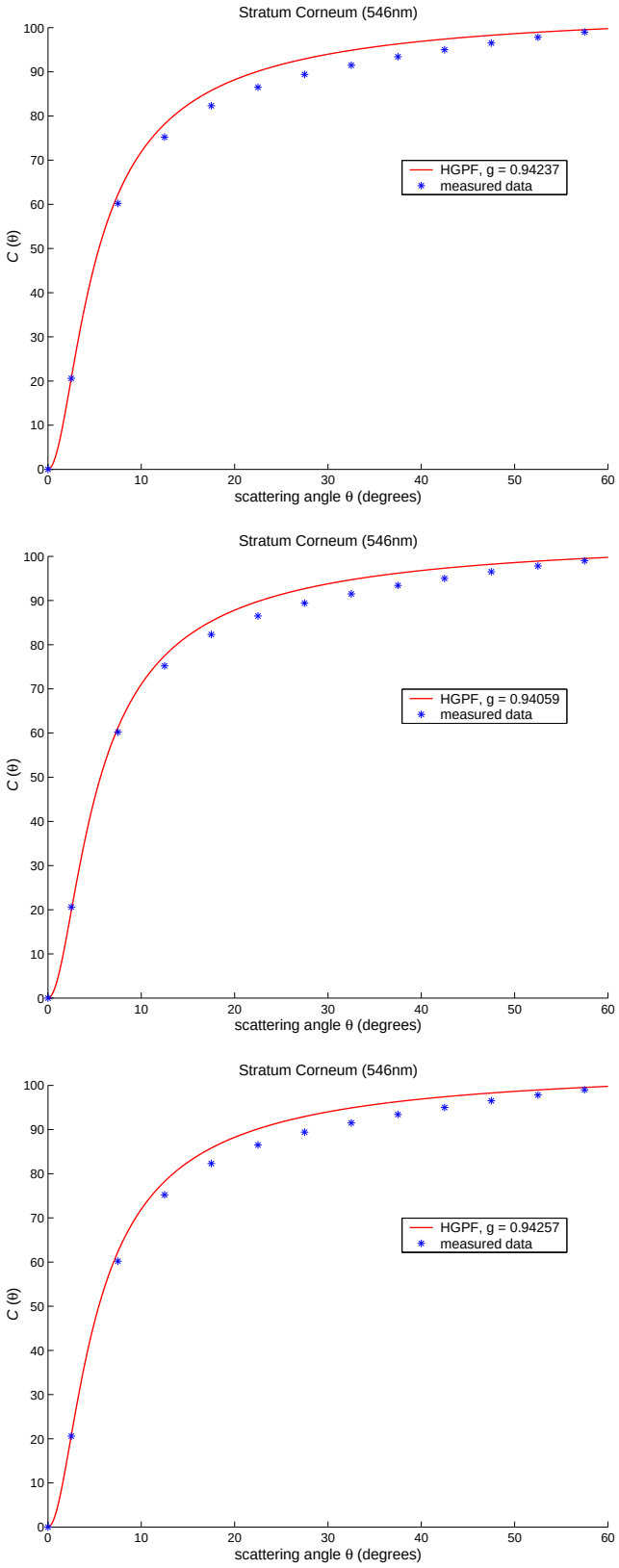

Figure 16: *Asymmetry factor computed using: absolute error (top), relative error (middle) and RMS error metric (bottom).*

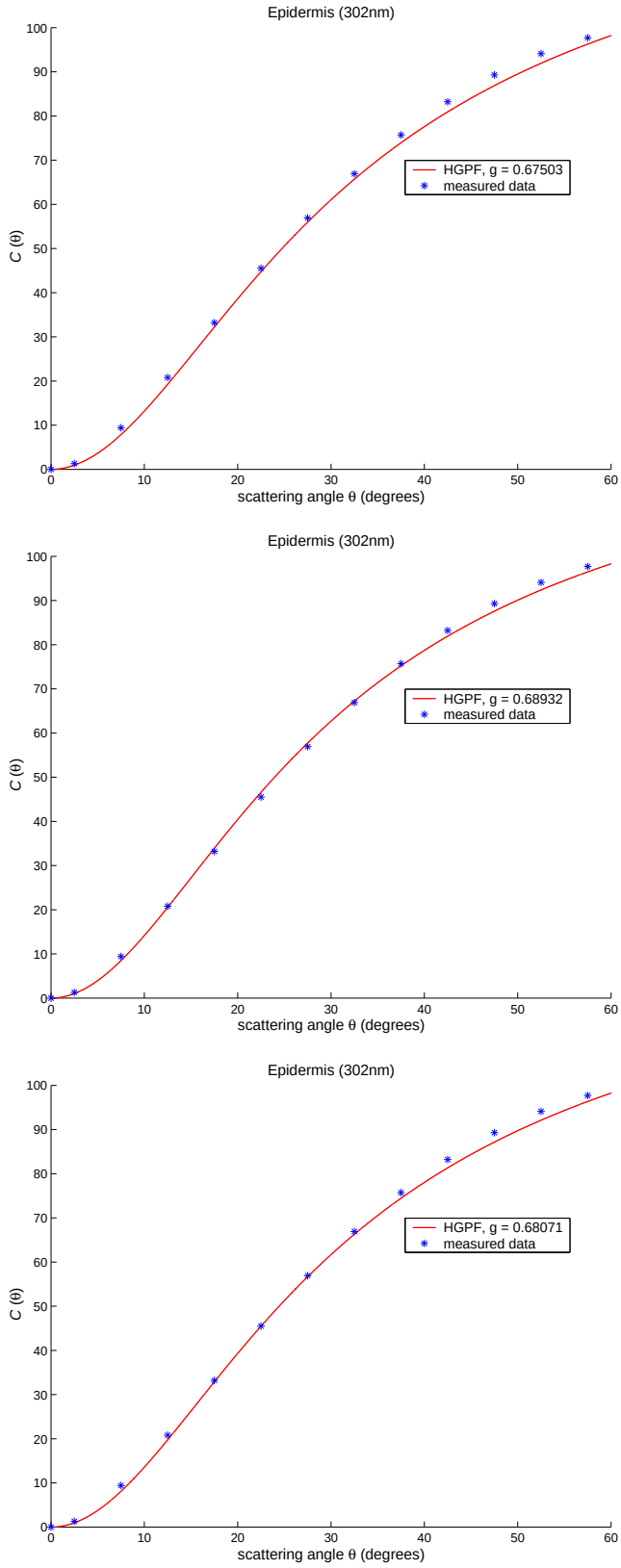

Figure 17: *Asymmetry factor computed using: absolute error (top), relative error (middle) and RMS error metric (bottom).*

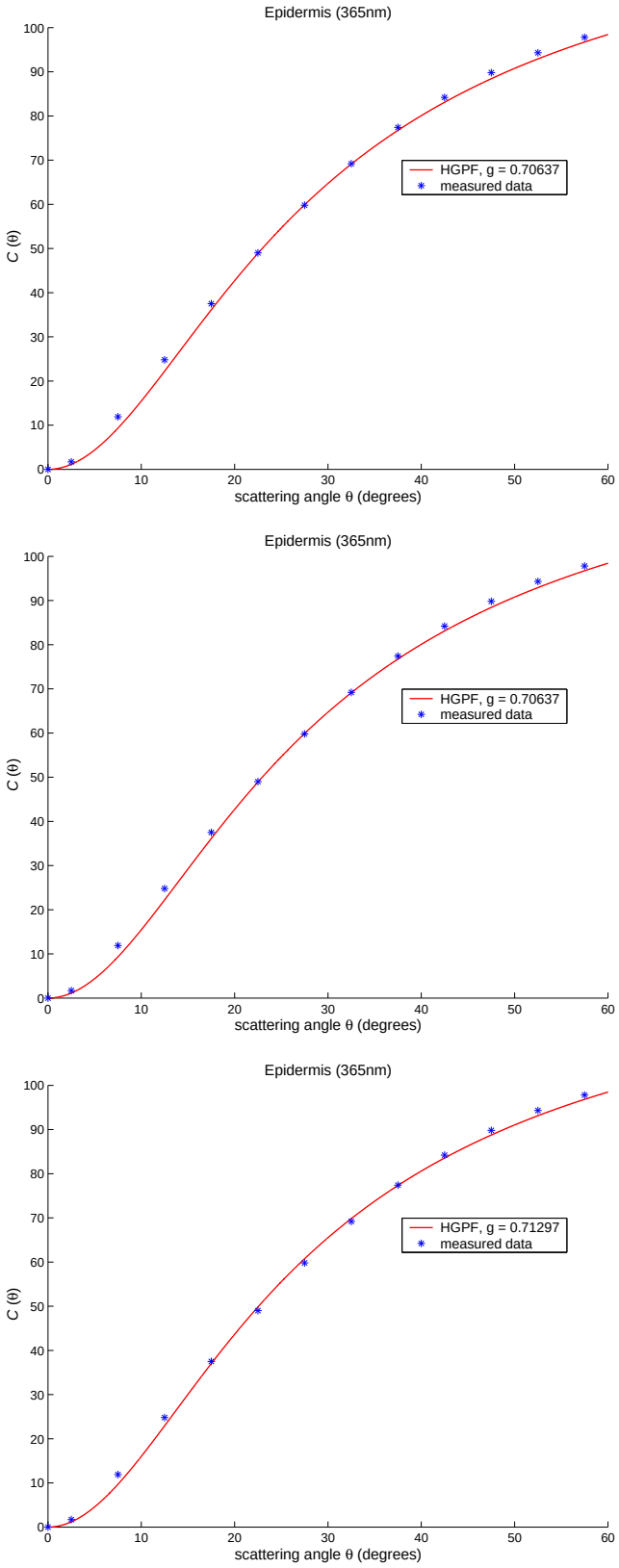

Figure 18: *Asymmetry factor computed using: absolute error (top), relative error (middle) and RMS error metric (bottom).*

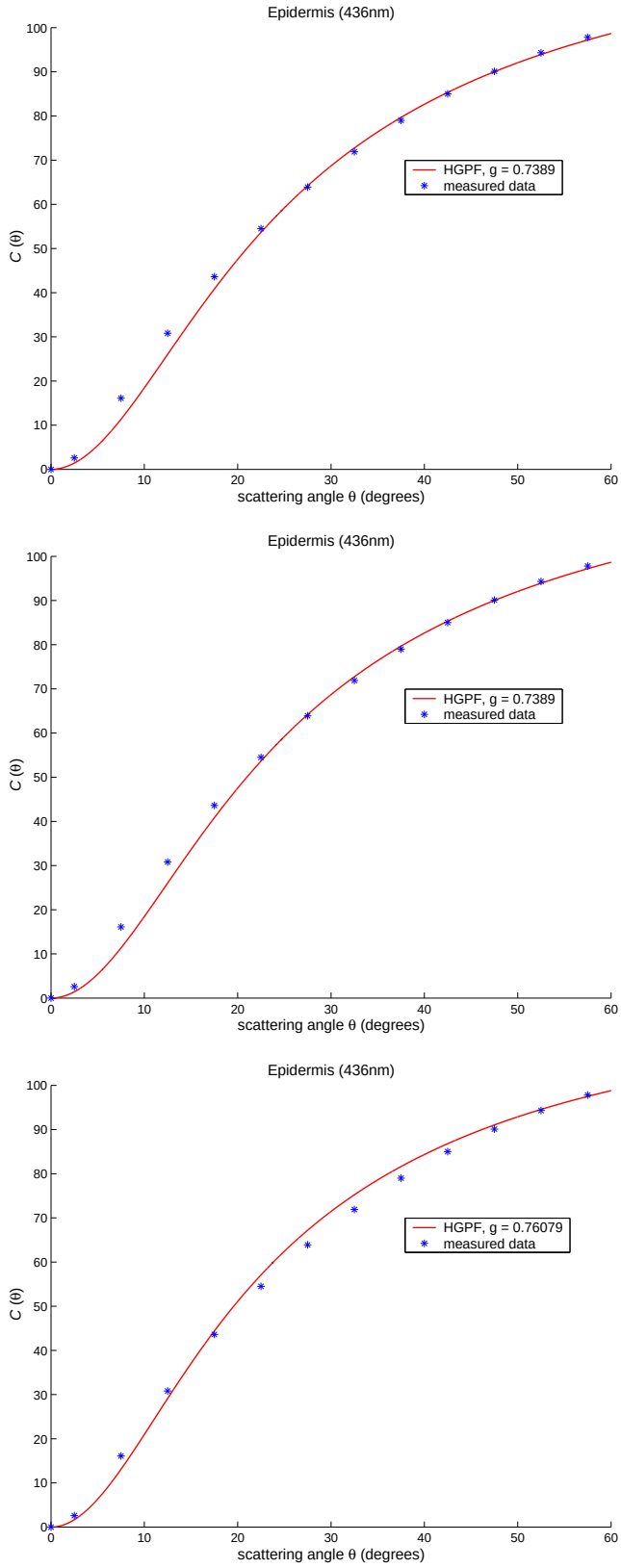

Figure 19: *Asymmetry factor computed using: absolute error (top), relative error (middle) and RMS error metric (bottom).*

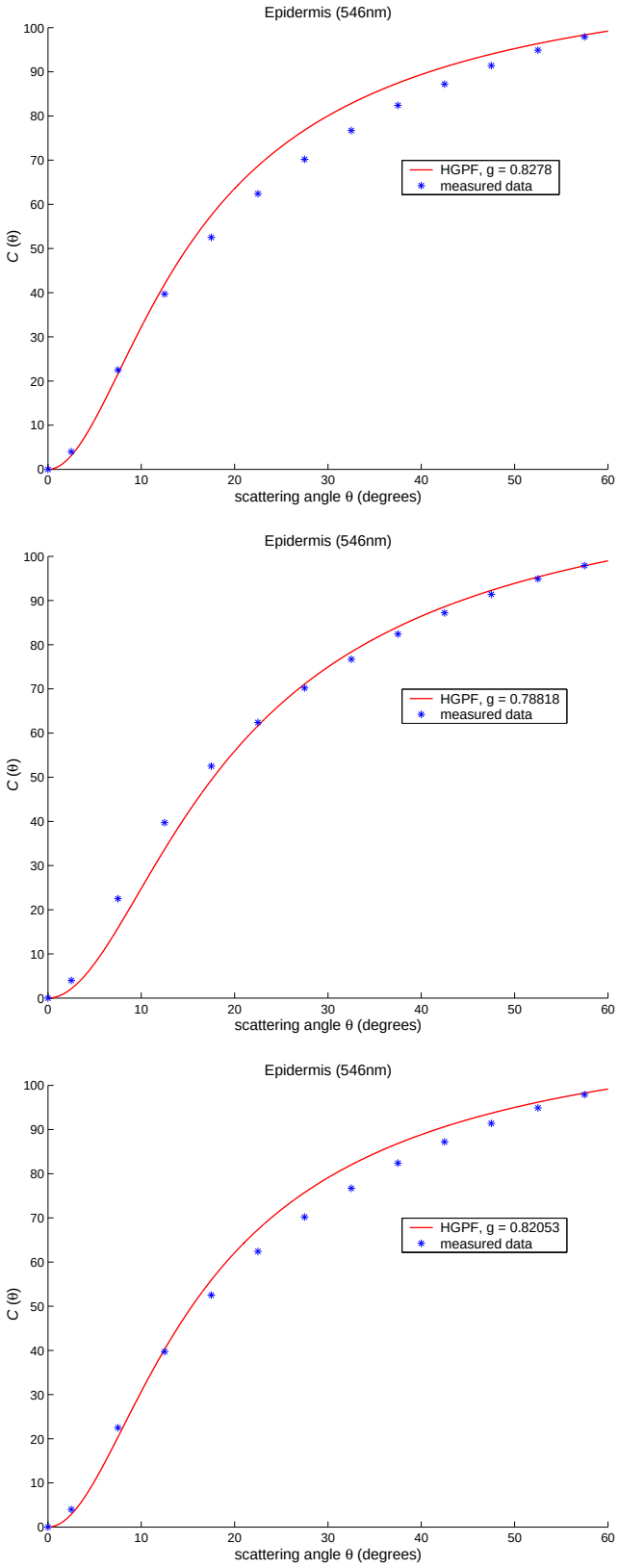

Figure 20: *Asymmetry factor computed using: absolute error (top), relative error (middle) and RMS error metric (bottom).*